Research Article | Open Access

Microstructures

Zhou et al. Microstructures 2026, 6, 2026090 DOI:10.20517/microstructures.2026.12

Hollow $Ni_{0.5}Zn_{0.5}Fe_2O_4$/C/Ni microspheres with excellent microwave absorption properties

Ding Zhou[1,2], Ruimin Shi[3], Chen Li[2], Anping Wang[2], Yu Gao[2], Qiang Wu[4], Qikui Man[2], Baogen Shen[2]

Keywords:
Ferrite, hollow microspheres, graphitization degree, microwave absorption

Citation: Zhou, D.; Shi, R.; Li, C.; Wang, A.; Gao, Y.; Wu, Q.; Man, Q.; Shen, B. Hollow $Ni_{0.5}Zn_{0.5}Fe_2O_4$/C/Ni microspheres with excellent microwave absorption properties. *Microstructures* **2026**, *6*, 2026090. https://dx.doi.org/10.20517/microstructures.2026.12

Received: 20 Jan 2026
First Decision: 4 Mar 2026
Revised: 30 Apr 2026
Accepted: 26 May 2026
Published: 30 Jun 2026

Academic Editors:
Xiaohui Liang, Dae-Yong Jeong
Copy Editor:
Ping Zhang
Production Editor:
Ping Zhang

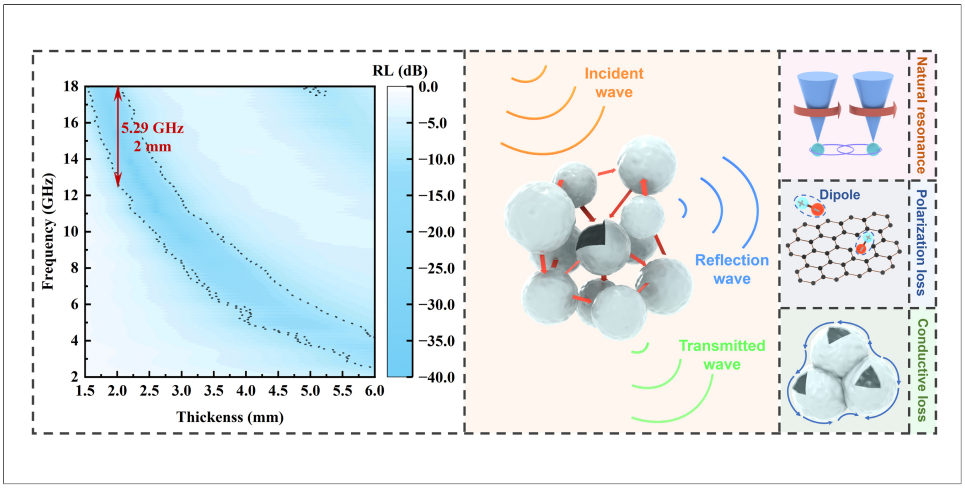

Abstract

The development of highly efficient microwave absorbers presents a significant challenge, driven by the growing issue of severe electromagnetic pollution. In this context, precise structural design emerges as a decisive factor for enhancing the microwave absorption capabilities. In this work, the hollow $Ni_{0.5}Zn_{0.5}Fe_2O_4$/C/Ni microspheres were fabricated through hydrothermal method, calcination treatment and further annealing. The results of the morphology observation demonstrate that the heterogeneous $Ni_{0.5}Zn_{0.5}Fe_2O_4$/C/Ni composites are hollow microspheres, consisting of many nanoparticles. Strikingly, the appearance of metallic Ni alongside increased carbon graphitization results from the partial reduction of Ni^{2+} by carbon during high-temperature annealing in the Ar atmosphere, which can be beneficial to the dielectric loss. The hollow $Ni_{0.5}Zn_{0.5}Fe_2O_4$/C/Ni microspheres possess outstanding microwave absorption capabilities, mainly owning to the better interface and dipole polarization, eddy current loss, conduction loss and natural resonance loss, multiply reflection and scattering between the microspheres. The hollow $Ni_{0.5}Zn_{0.5}Fe_2O_4$/C/Ni microspheres annealed at 700 °C exhibited an optimal reflection loss

[1]College of Chemical Engineering, Zhejiang University of Technology, Hangzhou 310014, Zhejiang, China.
[2]Zhejiang Key Laboratory of Magnetic Materials and Applications, Ningbo Institute of Materials Technology & Engineering, Chinese Academy of Sciences, Ningbo 315201, Zhejiang, China.
[3]School of Mathematics and Physics, Handan University, Handan 056005, Henan, China.
[4]Ningbo Fengci Technology Co., Ltd., Ningbo 315201, Zhejiang, China.

Correspondence to: Dr. Yu Gao, Prof. Qikui Man, Zhejiang Key Laboratory of Magnetic Materials and Applications, Ningbo Institute of Materials Technology & Engineering, Chinese Academy of Sciences, Ningbo 315201, Zhejiang, China. E-mail: gaoy@nimte.ac.cn; manqk@nimte.ac.cn.

(RL) value of -35.79 dB at 2.5 mm and an effective absorption bandwidth (EAB) of 5.29 GHz at 2.0 mm. The present study reveals a design approach for heterostructures, which offers novel insights into the fabrication of high-performance microwave absorbing materials.

INTRODUCTION

The remarkable advancements in electronic technology have undoubtedly brought about a significant degree of convenience for human beings. However, it is important to acknowledge the concomitant problems that have arisen, including but not limited to electromagnetic interference and radiation pollution[1-3]. In order to solve these critical issues, considerable efforts have been made to develop microwave absorption materials that exhibit a broad absorption bandwidth, a thin structure, a high degree of absorption, and a low weight[4-6]. Based on the electromagnetic wave (EMW) loss mechanism, EMW absorption materials can be categorized into two main types: dielectric loss-type and magnetic loss-type materials[7-10].Among many promising materials, ferrites, especially the spinel ferrites, exhibit excellent electromagnetic properties, including high saturation magnetization, high magnetic crystal anisotropy, high Curie temperature and reliable chemical stability[11-13]. However, the ferrite-based absorbers usually present a high filling ratio and a heavy coating, which greatly limits their military and practical application[13-15]. Fortunately, this issue can be efficiently addressed through the combination of ferrites and low-density materials with excellent dielectric properties[16,17]. For example, Tang *et al.*[18] reported the development of a zinc ferrite/multi-walled carbon nanotubes (MWCNTs) composite using a combined co-hydrothermal and sol-gel approach, with an optimal reflection loss (RL) of -40.65 dB achieved at 0.81 GHz. Zong *et al.*[19] reported a maximum RL of -47.8 dB at 10.7 GHz for their reduced graphene oxide-$Ni_{0.5}Zn_{0.5}Fe_2O_4$ composite, which was produced via a simple approach. Zhou *et al.*[20] fabricated carbon nanotube/$Ni_{0.5}Zn_{0.5}Fe_2O_4$ composite by a combined precipitation-hydrothermal method, exhibiting a strong RL value of -32.5 dB at 3.9 GHz.

Furthermore, another determinant for adjusting EMW absorption performance lies in the morphology and structural design of the materials themselves. Extensive research has confirmed that hollow structures not only alleviate the weight of ferrite-based coatings, but also enhance their electromagnetic performance[21-23]. It is feasible to summarize the advantages of hollow ferrite structures as: (i) enhanced impedance matching, (ii) reduced the filling ratio to achieve material lightweighting, and (iii) reinforced interfacial polarization[24]. For instance, Sui *et al.*[25] fabricated hollow Fe_3O_4 particles by solvothermal method, which exhibited the effective absorption bandwidth (EAB) of 4.72 GHz at 2.49 mm. Moreover, the RL of -55.14 dB was attained at a matching thickness of 2.07 mm. Mandal *et al.*[26] prepared $NiFe_2O_4$ nano-hollow spheres via a solvothermal process, which demonstrated an EAB of 2.82 GHz at a thickness of 2 mm and a strong RL of -59.2 dB at 11.7 GHz. Zhu *et al.*[27] obtained hollow Fe/Fe_3O_4@porous carbon composites, exhibiting an EAB of 5.20 GHz and an RL of -50.05 dB.

Both the incorporation of ferrite with high dielectric materials such as nickel, zinc, and carbon, and the design of hollow structures demonstrate distinct advantages. Using these two methods in combination will maximize the microwave absorption properties of the obtained material. Thus, the $Ni_{0.5}Zn_{0.5}Fe_2O_4$/C hollow microspheres were prepared by self-sacrifice processing and annealing treatment. These hollow microspheres are further characterized, with their morphology, crystalline structure, and microwave electromagnetic performance being investigated as a function of annealing temperature. This $Ni_{0.5}Zn_{0.5}Fe_2O_4$/C hollow microsphere is a ternary composite material. Under the interfacial polarization effects between Ni-Zn ferrite, carbon, and nickel, the composite exhibits multiple loss mechanisms, delivering excellent impedance matching and absorptive properties while achieving the integration of various single-type materials. This work offers a novel strategy for preparing high-performance ferrite-based microwave absorbers.

MATERIALS AND METHODS

Materials

The fabrication of $Ni_{0.5}Zn_{0.5}Fe_2O_4$/C/Ni hollow microspheres involved a simple hydrothermal method and subsequent calcination. First, a homogeneous solution was prepared by dissolving 7.5 g of glucose, 1.471 g of $(NH_4)_2Fe(SO_4)_2{\cdot}6H_2O$, 0.269 g of $ZnSO_4{\cdot}7H_2O$, and 0.246 g of $NiSO_4{\cdot}6H_2O$ in 50 mL of deionized water. The resulting homogeneous solution was diverted to a 100 mL Teflon-lined stainless steel autoclave and heated at 160 °C for 24 h to undergo a hydrothermal reaction. Upon reaching room temperature, the obtained precipitates underwent repeated washing with deionized water and subsequent drying in air at 80 °C for 6 h. Calcination of this material at 400 °C for 4 h (1 °C·min^{-1}), and the $Ni_{0.5}Zn_{0.5}Fe_2O_4$/C hollow microspheres were obtained. At last, the $Ni_{0.5}Zn_{0.5}Fe_2O_4$/Ni/C microstructure was obtained by annealing under Ar atmosphere at 600, 700, 800 °C for 2 h. In this work, the prepared $Ni_{0.5}Zn_{0.5}Fe_2O_4$/C composite is designated as S1; the samples subsequently annealed at 600, 700, and 800 °C are correspondingly labeled S2, S3, and S4.

All chemical reagents were of analytical grade and used as received without further purification. Glucose (96%), $(NH_4)_2Fe(SO_4)_2{\cdot}6H_2O$ (99.99%), and $ZnSO_4{\cdot}7H_2O$ (99.995%) were purchased from Aladdin Biochemical Technology Co., Ltd. (Shanghai, China). $NiSO_4{\cdot}6H_2O$ (99.9%) were purchased from Macklin Biochemical Co., Ltd. (Shanghai, China).

Characterization

A Bruker D8 Advance diffractometer (Bruker, Germany) equipped with Cu-Kα radiation (λ = 0.154 nm) was used for X-ray diffraction (XRD) analysis. The scans were recorded over a 2θ range of 5° to 90°. A Hitachi S4800 scanning electron microscopy (SEM, Hitachi, Japan) and an Field Electron and Ion (FEI) Tecnai F20 transmission electron microscope (TEM, FEI Company, USA) were used to investigate the morphological and microstructural characteristics. Raman spectra were recorded at room temperature on a Renishaw inVia Reflex spectrometer (Renishaw, UK), covering the wavenumber range from 100 cm^{-1} to 1,800 cm^{-1}. The chemical states of surface metal atoms were investigated by X-ray photoelectron spectroscopy (XPS), using an Axis Ultra Delay-Line Detector (DLD) spectrometer (Kratos, UK). To measure the electromagnetic absorption properties, the composites were incorporated into paraffin wax at a mass fraction of 20% and molded into circular rings of 7 mm outer diameter with a 3.4 mm inner diameter. Measurement of both the complex permittivity and permeability for the ring-shaped samples was conducted in the 2-18 GHz band with an Agilent N5234A vector network analyzer (VNA, Keysight Technologies, USA).

RESULTS AND DISCUSSION

XRD was employed to investigate the crystal structure of each sample, with the resulting patterns presented in Figure 1A. The cubic-structured $Ni_{0.5}Zn_{0.5}Fe_2O_4$ (JCPDS 08-0234) is identified by the diffraction peaks marked ★. The corresponding characteristic peaks at 18.3°, 30.0°, 35.4°, 37.0°, 43.0°, 53.3°, 56.8°, 62.4°, 70.8°, and 73.8° correspond to the (111), (220), (311), (222), (400), (422), (511), (440), (620), and (533) crystal planes, respectively[28]. Meanwhile, the diffraction peaks marked ▼ are attributed to the face-centered cubic structure Ni (JCPDS 65-0308), with the characteristic peaks at 44.4°, 51.7°, and 76.2° being indexed to its (111), (200), and (220) planes, respectively[29]. The XRD diffraction spectra of S1 shows the weak diffraction peaks, indicating poor crystallinity of $Ni_{0.5}Zn_{0.5}Fe_2O_4$. The broad diffraction peak at 10°-20° of S1 attributed to amorphous carbon[30]. For sample S2, S3 and S4, the diffraction peaks of carbon gradually become weaker as annealing temperature increases, showing the content of carbon decreases. The characteristic peaks of the $Ni_{0.5}Zn_{0.5}Fe_2O_4$ become sharper, indicating the $Ni_{0.5}Zn_{0.5}Fe_2O_4$ is well crystallized. As the temperature increases, the diffraction peaks associated with metallic Ni grow progressively, indicating the development of higher crystallinity at elevated temperatures. During high-temperature annealing under the Ar atmosphere, metallic Ni results from the reduction of Ni^{2+} by carbon[31].

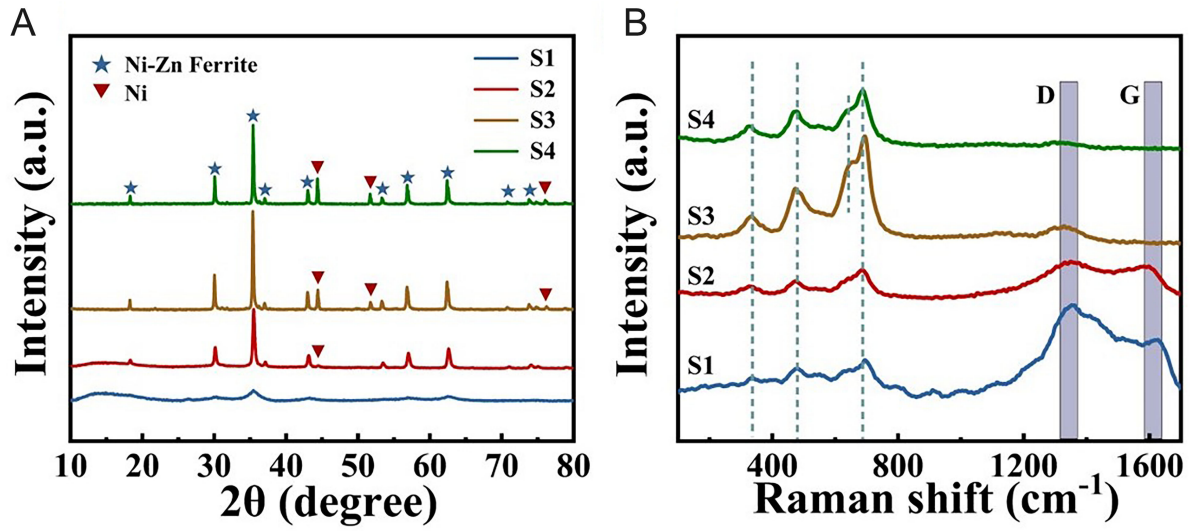

Figure 1. XRD diffraction spectra (A), Raman spectra of all samples (B).

Figure 1B shows the Raman spectra for all samples, spanning from 100 cm^{-1} to 1,700 cm^{-1}. There are five major Raman active modes ($A_{1g} + E_g + 3T_{2g}$), however, only 3 modes peaks are detected[32]. The Raman peaks located at ~330, ~470, and ~690 cm^{-1} assign to the E_g, T_{2g}, and A_{1g} modes, respectively[33]. The splitting of the A_{1g} mode into the $A_{1g}(1)$ and $A_{1g}(2)$ branches arises from an alteration in structural symmetry, caused by the reordering of Ni^{2+},Zn^{2+} and Fe^{3+}[34]. In addition, two prominent bands are observed: one centering on ~1,327 cm^{-1}, attributed to sp^3 defects; and the other at ~1,594 cm^{-1}, corresponding to the in-plane vibrations of sp^2 bonded carbon[35]. For samples S3 and S4, the D and G bands are difficult to identify in Figure 1B, indicating a low carbon content, which is consistent with the XRD results. The measured D/G peak intensity ratios (I_D/I_G) for the four samples are 1.67 (S1), 1.09 (S2), 1.04 (S3), and 0.95 (S4). This ratio serves as a standard indicator for assessing the graphitization level of carbon materials. The notably high value for S1 (1.67) indicates a predominantly amorphous carbon structure with low graphitization[36]. And the decline in the I_D/I_G ratio with increasing annealing temperature reflects an enhancement in the graphitization degree of the carbon components.

Figure 2A-D display the SEM morphology of all samples, which consist of numerous microspheres. The presence of fractured microspheres reveals their hollow structure. The average particle diameters were determined to be 1.058 ± 0.160, 0.972 ± 0.237, 0.689 ± 0.148, and 0.561 ± 0.142 μm for S1, S2, S3, and S4, respectively. These size distributions are illustrated in Figure 3. As the temperature rises, the hollow microspheres undergo volumetric contraction. This shrinkage is primarily due to the densification of adsorbed metal ions into oxides and the further carbonization of organic matter during heat treatment[37].

The TEM, high-resolution transmission electron microscopy (HRTEM) and selected area electron diffraction (SAED) are investigated to understand the morphology of samples. TEM micrographs in Figure 2E-H show that these microspheres possess a hollow structure constructed from numerous nanoparticles. The HRTEM images Figure 2I-L reveal no discernible lattice fringes in sample S1, confirming its poor crystallinity. The observed lattice fringes in samples S2, S3, and S4 correspond to the (111) crystallographic plane of $Ni_{0.5}Zn_{0.5}Fe_2O_4$, with interplanar distances measured as 0.484, 0.485, and 0.486 nm, respectively. Additionally, a lattice fringe of 0.253 nm is observed in sample S3, which corresponds to the (311) plane of $Ni_{0.5}Zn_{0.5}Fe_2O_4$. As displayed in Figure 2M-P, the SAED pattern of S1 shows no obvious diffraction rings. And the SAED pattern of S2 exhibiting sharp and discrete rings can be matched with the (111), (220), (311) and (400)

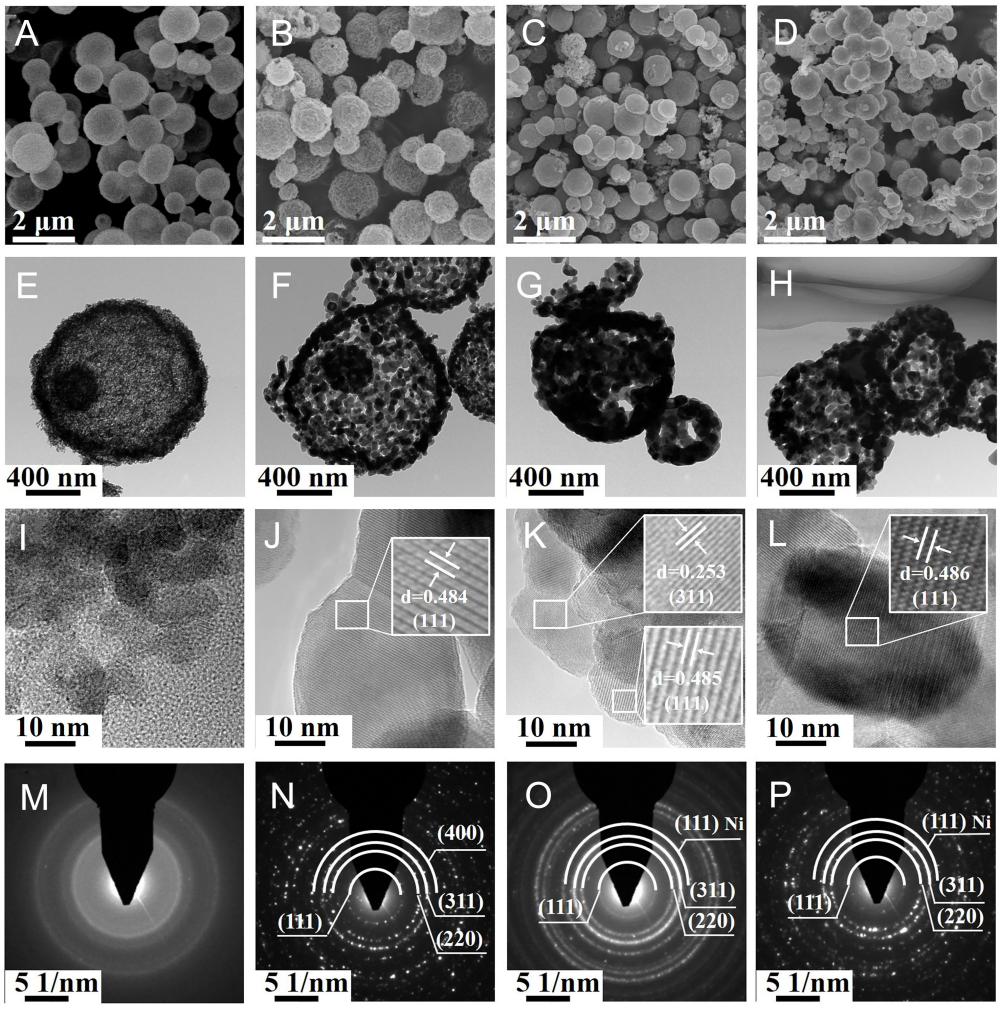

Figure 2. SEM images of S1 (A), S2 (B), S3 (C), S4 (D). TEM images of S1 (E), S2 (F), S3 (G), S4 (H); HRTEM images of S1 (I), S2 (J), S3 (K), S4 (L) and SAED spectrum of S1 (M), S2 (N), S3 (O), S4 (P). SEM: Scanning electron microscopy; TEM: transmission electron microscope; HRTEM: high-resolution transmission electron microscopy.

planes, which is consistent with the planes of $Ni_{0.5}Zn_{0.5}Fe_2O_4$. Moreover, the appearance of diffraction ring according with (111) plane of Ni can be observed in S3 and S4, further indicating the existence of metallic Ni.

Elemental mapping of samples S1-S4 [Figure 4] serves to examine the effect of annealing temperature on the composition distribution of Fe, Ni, Zn, O, and C. The red flaky areas belong to the substrate used in the TEM preparation process rather than the sample. As shown, the Zn, Fe, O, and C elements exhibit a homogeneous distribution on the microsphere surfaces. As the annealing temperature rises, the distribution of element C decreases, corresponding to a lower surface carbon content. In contrast, Ni tends to aggregate towards the particle surface, especially in sample S4. This illustrates the partial carbothermal reduction of $Ni_{0.5}Zn_{0.5}Fe_2O_4$ to metallic Ni by amorphous carbon.

The elemental composition and chemical states of samples S1-S4 are analyzed by XPS. Figure 5 shows Ni $2p_{3/2}$ spectrum, the peaks at around 853.5, 855.0, and 856.6 eV are attributed to satellite peak of Ni^{0+}, Ni^{2+} in the octahedral site [$Ni^{2+}(O_h)$] and Ni^{2+} in the tetrahedral site [$Ni^{2+}(T_d)$], respectively[38]. Strikingly, a low-valence Ni^{0+} peak can be detected in S2, S3 and S4, confirming that Ni^{2+} in the $Ni_{0.5}Zn_{0.5}Fe_2O_4$ is partly reduced to metallic Ni[39]. Meanwhile, the increased peak intensity of Ni^{0+} as temperature increasing indicates

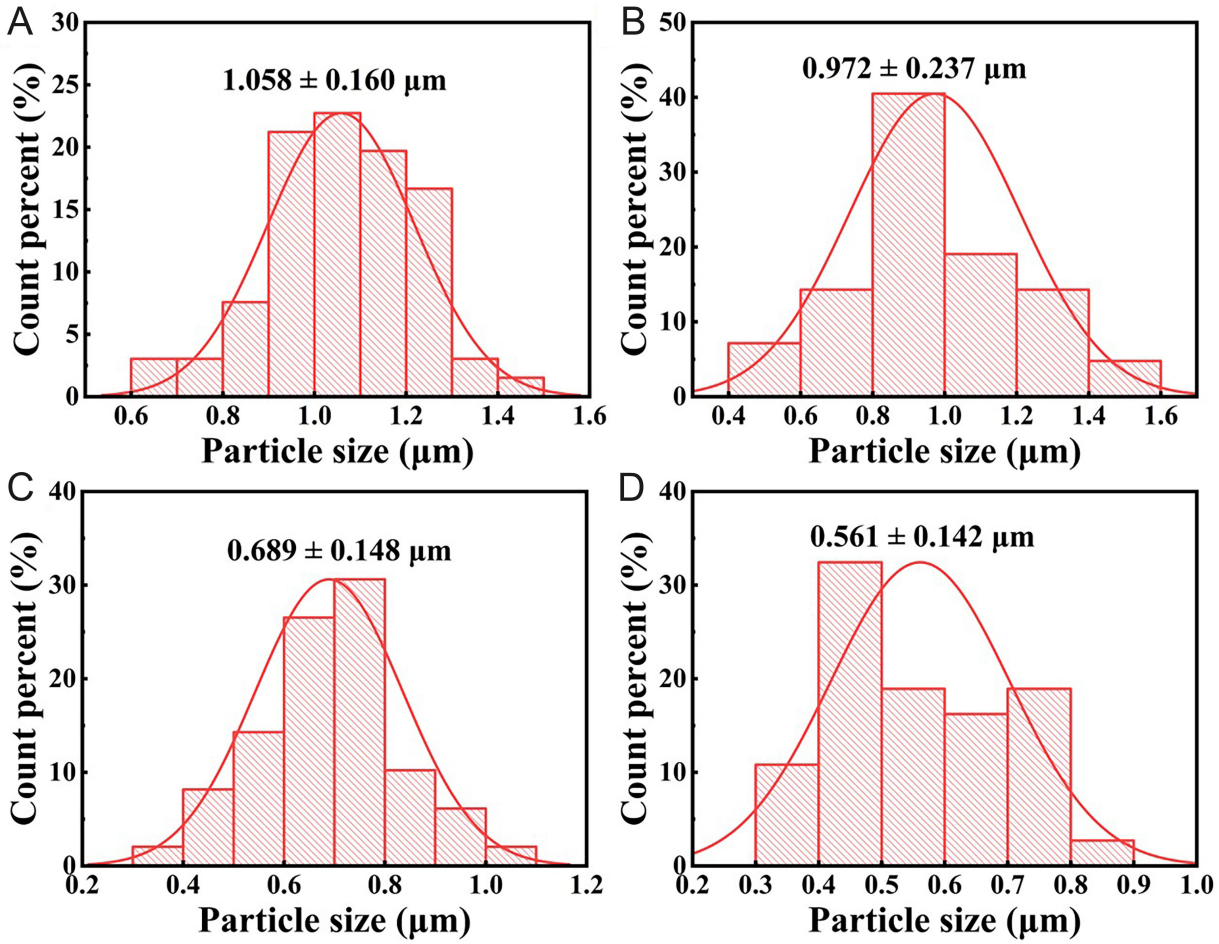

Figure 3. Particles size distribution of S1 (A), S2 (B), S3 (C) and S4 (D).

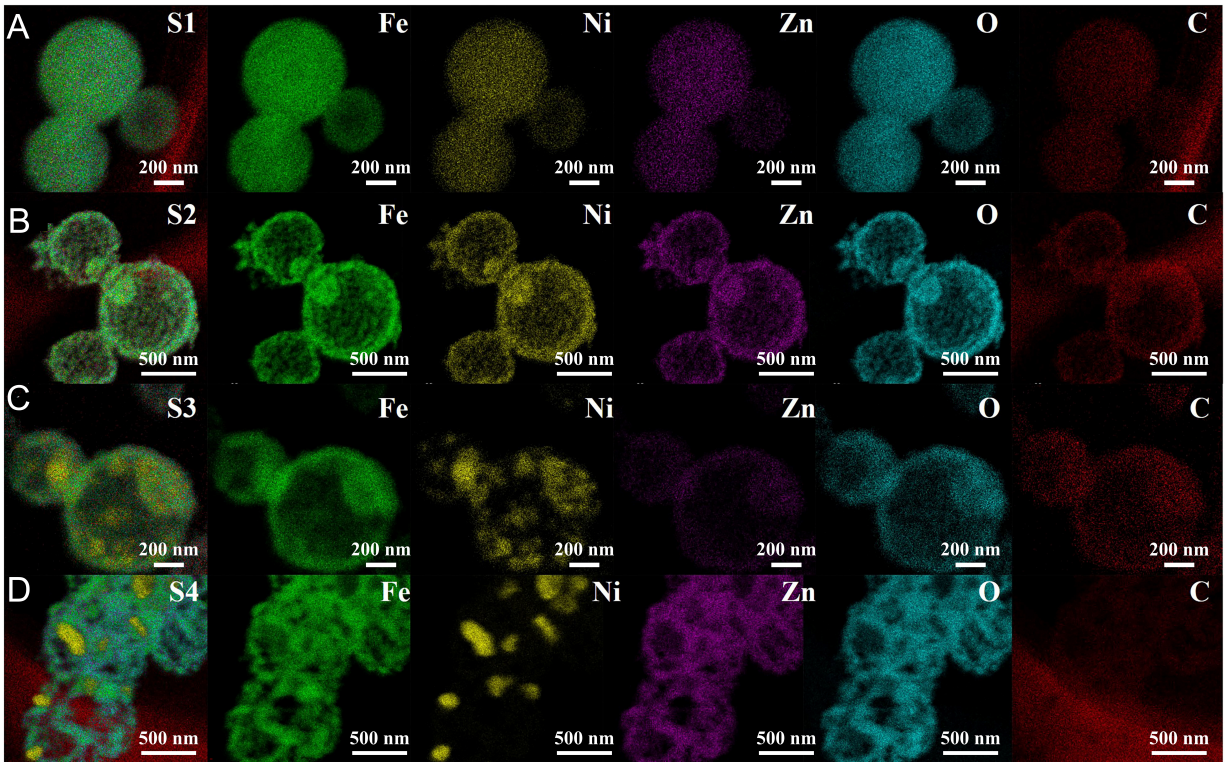

Figure 4. Elemental mapping images of S1 (A), S2 (B), S3 (C), S4 (D).

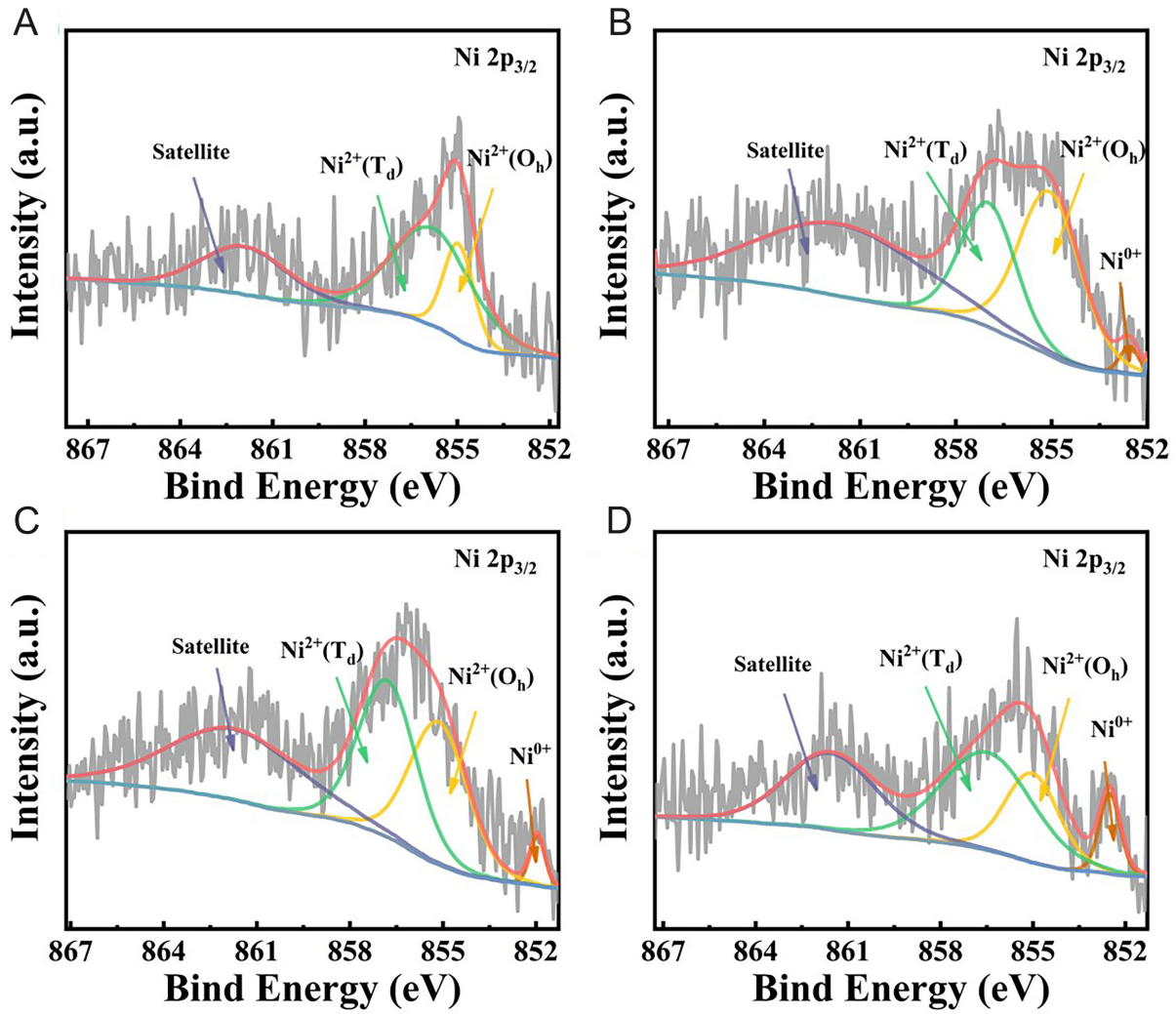

Figure 5. XPS spectra of Ni 2p of S1 (A), S2 (B), S3 (C), S4 (D). XPS: X-ray photoelectron spectroscopy.

more Ni^{2+} is reduced to metallic Ni, a finding that corresponds to the XRD data. The C 1s XPS spectra [Figure 6] are fitted with three peaks at approximately 284.8, 288.8, and 286.0 eV, ascribed to C-C/C=C, C-O, and C=O functional groups, respectively[40]. The C-C/C=C peak is the most intense, and its area decreases with increasing annealing temperature. This decrease reflects a progressive graphitization of the carbon components as the annealing temperature increases. As shown in the Figure 7, the Fe 2p XPS spectra exhibits characteristic satellite peaks. The peak at approximately 718.6 eV is associated with the Fe $2p_{3/2}$ component, while the one at about 733.2 eV belongs to the Fe $2p_{1/2}$ component. Each of the Fe $2p_{3/2}$ and Fe $2p_{1/2}$ bands was deconvoluted into two component peaks. For the Fe $2p_{3/2}$ region, the peaks at 710.5 eV and 712.2 eV are attributed to Fe^{2+} and Fe^{3+} states, respectively. Similarly, the Fe $2p_{1/2}$ peaks at 723.7 eV and 725.4 eV are assigned to Fe^{2+} and Fe^{3+}[41]. The Fe^{2+} area ratio of Fe element in XPS can be used to measure the variation trend of Fe^{2+} in ferrite with annealing temperature. The corresponding Fe^{2+} area ratios for the four samples (S1-S4) are 0.38, 0.51, 0.53, and 0.52. This increase mainly because when Ni^{2+} is reduced to metallic Ni, Fe^{3+} will replace the Ni^{2+} sites and become Fe^{2+}.

The complex permittivity ($\varepsilon_r = \varepsilon' - j\varepsilon''$) and dielectric loss tangent of the samples are presented in Figure 8A-C, whereas their complex permeability ($\mu_r = \mu' - j\mu''$) and magnetic loss tangent are shown in Figure 8D-F. The energy storage capacity within a material is respectively represented by the real parts of its complex

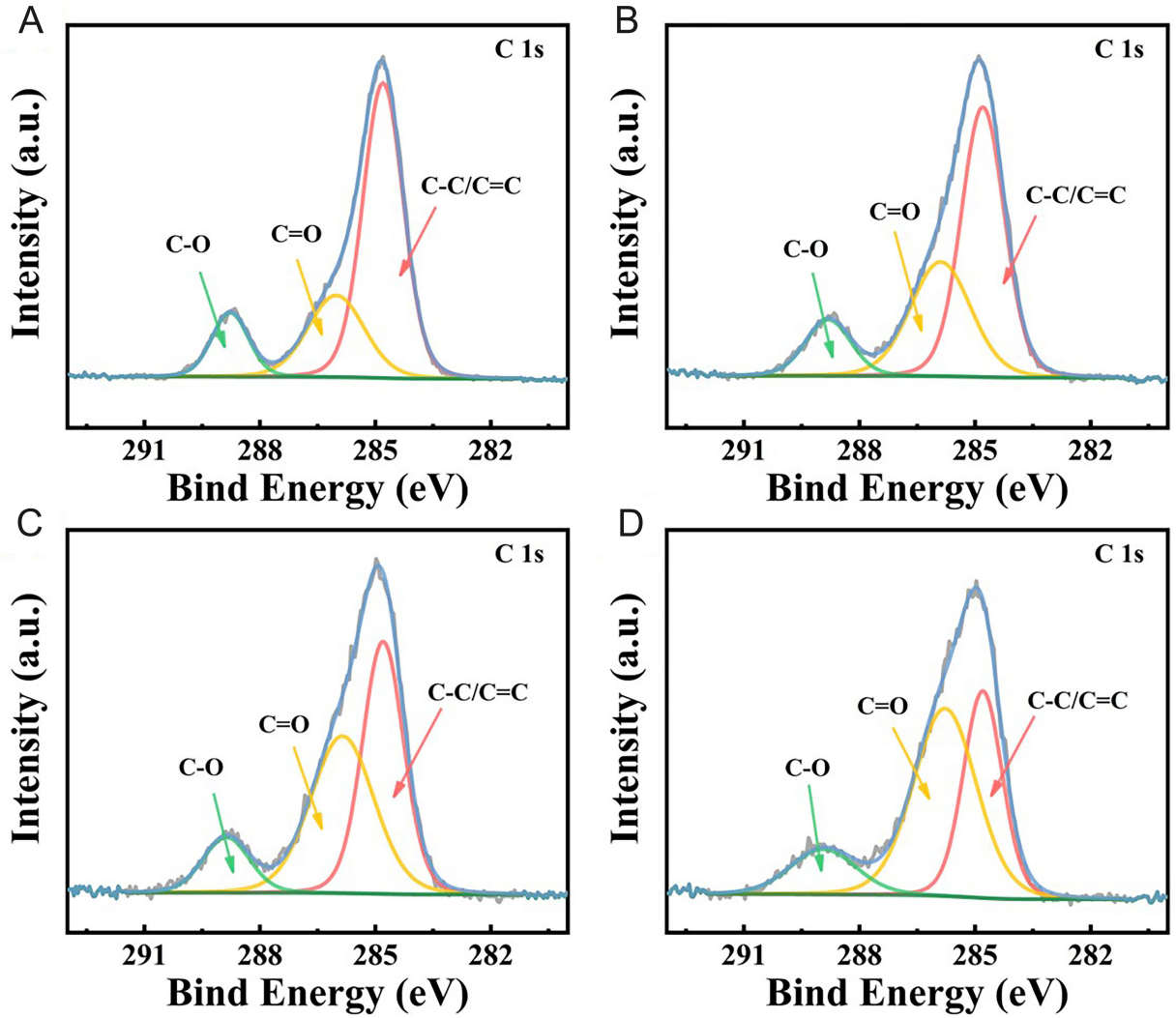

Figure 6. XPS spectra of C 1s of S1 (A), S2 (B), S3 (C), S4 (D). XPS: X-ray photoelectron spectroscopy.

permittivity (ε') for electric energy and permeability (μ') for magnetic energy. Conversely, the dissipation of electric and magnetic energy is respectively reflected in the imaginary parts ε'' and μ''[42]. Notably, for sample S1, both the permittivity and permeability are not only the lowest but also show minimal variation across the frequency range, pointing to a limited dielectric loss capability. A clear upward trend in both ε' and ε'' is observed for samples S2, S3, and S4. The reasons for this enhancement in complex permittivity are as follows: (1) During the formation of $Ni_{0.5}Zn_{0.5}Fe_2O_4$/C hollow microspheres at high temperature, the enhanced crystallization of carbon facilitates the generation of polar bonds and polarization charges, leading to the increase in electrical conductivity (δ)[43]. As dictated by the classical free electron theory ($\varepsilon'' = \delta / 2\pi\varepsilon_0 f$), the value of ε'' scales linearly with the electrical conductivity (δ)[24]. (2) The appearance of metallic Ni can lead to the increase of complex permittivity[44]. Therefore, as the annealing temperature rises and the metallic Ni content correspondingly increases, sample S4 achieves the largest dielectric imaginary part. This value is nearly double that observed in S2 and S3. In addition, as indicated by the preceding XRD results and Raman spectra, the graphitization degree of S2 has increased while the carbon content of S3 has decreased. Consequently, the ε' and ε'' values of S2 have risen, whereas the reduction in carbon content for S3 has led to a decrease in its ε' and ε'' values. Overall, the variation in permittivity results from the combined effects of metallic Ni content, carbon content, and carbon crystallinity/graphitization degree. As frequency increases, the μ' values of samples S2-S4 exhibit a decrease within the 2-8 GHz band before gradually converging

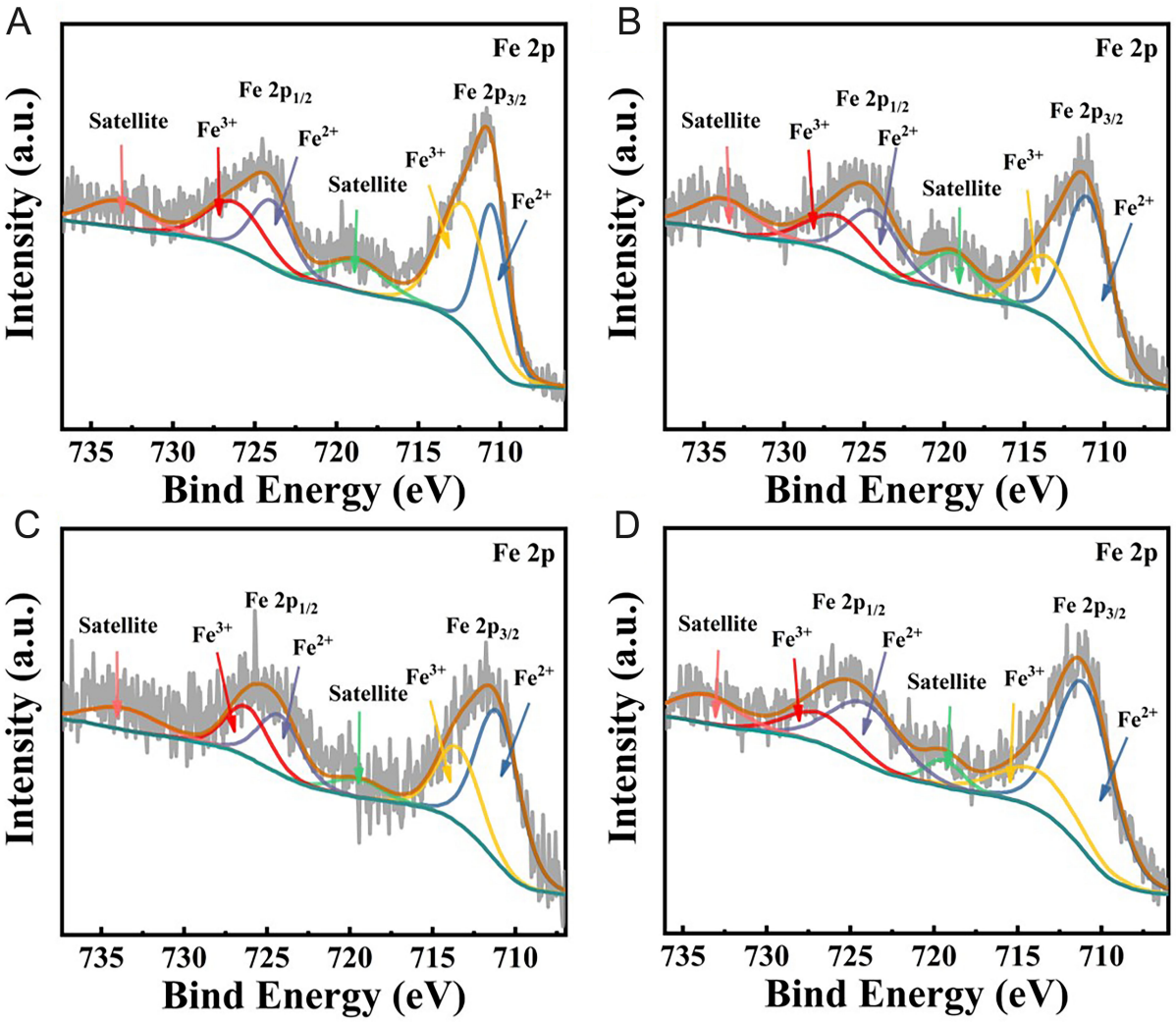

Figure 7. XPS spectra of Fe 2p of S1 (A), S2 (B), S3 (C), S4 (D). XPS: X-ray photoelectron spectroscopy.

toward 1, while those of S1 remain around 1 with only minor fluctuations, as depicted in Figure 8D. The values of μ" decrease significantly during 2-14 GHz and basically stay 0 at 14-18 GHz for S2-S4. The decline in permeability is primarily governed by the Snoek limit, which posits that the product of permeability and cut-off frequency is approximately constant. This relationship is formally described by the following equation[45]:

$$(\mu' - 1)\, f_c = \gamma M_s / 3\pi \quad (1)$$

Here μ' denotes the initial permeability, f_c represents the cut-off frequency, γ stands for the gyromagnetic ratio, and M_s signifies the saturation magnetization. As inferred from Equation (1), a higher permeability of the material corresponds to a lower cut-off frequency. Ni is a ferromagnetic material with a M_s higher than that of ferrite. Consequently, the incorporation of metallic Ni not only enhances the permeability of the sample but also elevates its cut-off frequency relative to ferrite. For this reason, while permeability decreases sharply in the high-frequency regime, the introduction of metallic Ni slightly shifts the cut-off frequency toward higher frequencies, which mitigates the rapid attenuation of permeability to a certain extent. This observation aligns with the results presented in Figure 8E.

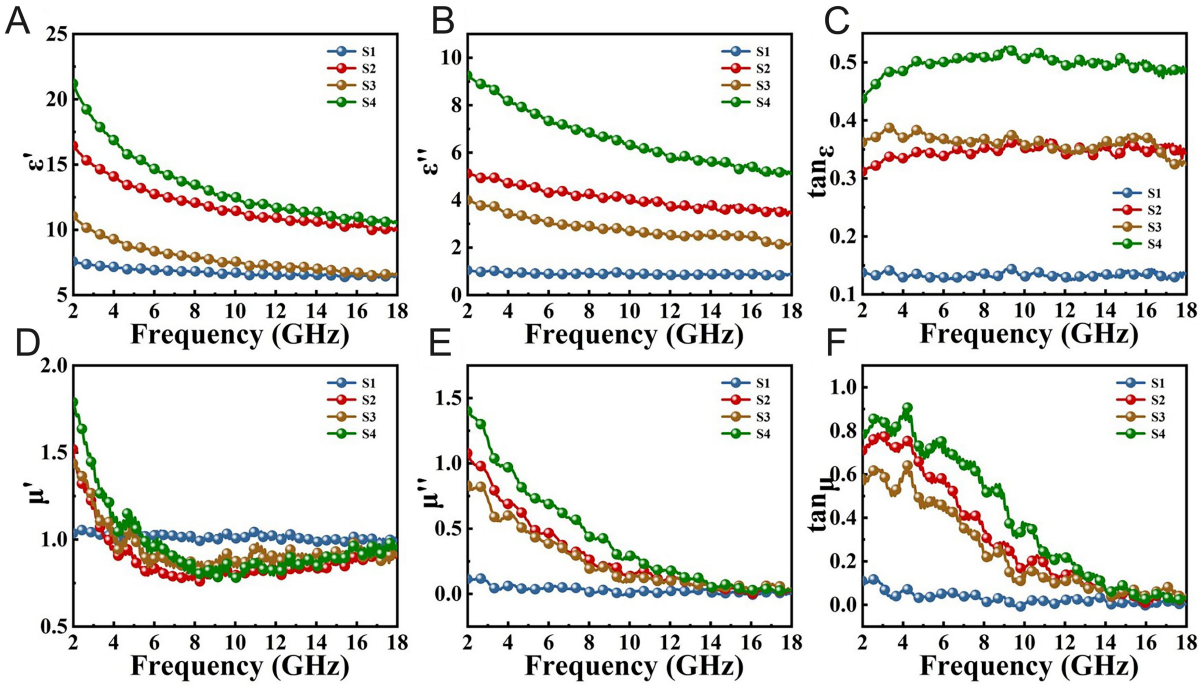

Figure 8. (A) Real parts of complex permittivity, (B) imaginary parts of complex permittivity, (C) dielectric loss tangents, (D) real parts of complex permeability, (E) imaginary parts of complex permeability, and (F) magnetic loss tangents of S1, S2, S3 and S4, respectively.

To elucidate the microwave absorption mechanism, the dielectric ($tan\delta_\varepsilon = \varepsilon''/\varepsilon'$) and magnetic ($tan\delta_\mu = \mu''/\mu'$) loss tangents of the samples were analyzed. As presented in Figure 8C, the $tan\delta_\varepsilon$ of S4 surpasses that of all other samples, indicating its strongest dielectric loss. Concurrently, the $tan\delta_\varepsilon$ for all samples exhibits fluctuations with increasing frequency. Regarding the characteristics of magnetic loss, as shown in Figure 8F, the S4 sample exhibits the highest $tan\delta_\mu$ value among samples S1-S4. A direct comparison between $tan\delta_\mu$ and $tan\delta_\varepsilon$ shows that within the 2-8 GHz range, $tan\delta_\mu$ exceeds $tan\delta_\varepsilon$, while from 8 GHz to 18 GHz, $tan\delta_\varepsilon$ is higher than $tan\delta_\mu$. This comparison indicates that magnetic loss dominates in the lower frequency band (2-8 GHz), whereas dielectric loss prevails in the higher frequency band (8-18 GHz).

In absorbing materials, the relaxation during polarization process is the primary source of dielectric loss. This process comprises multiple mechanisms: interfacial polarization, dipole orientation polarization, ionic polarization, and electron polarization[27]. Since ion and electron polarization are effective within the 10^3-10^6 Hz range, their contribution is negligible at microwave frequencies. The multiple loss mechanisms operating at these higher frequencies are commonly analyzed using Debye theory. The following equation characterizes the behavior of the complex permittivity[46]:

$$(\varepsilon' - \varepsilon_\infty)^2 + (\varepsilon'')^2 = (\varepsilon_s - \varepsilon_\infty)^2 \quad (2)$$

Here, ε_∞ and ε_s denote the relative permittivity and static permittivity, respectively. In generally, a Debye relaxation process is indicated by each semicircle observed in the Cole-Cole plot (ε' - ε'').

Figure 9A-D show the ε' - ε'' plots of samples S1, S2, S3 and S4, it is clear that Cole-Cole curves of S2, S3 and S4 consists of semicircles and straight tails. Such straight tails in S2, S3 and S4 are regarded as the evidence of the contribution of conduction loss, which is mainly brought out by the carbon[47]. It is well established that interfacial polarization significantly contributes to EMW relaxation losses in composite materials, as

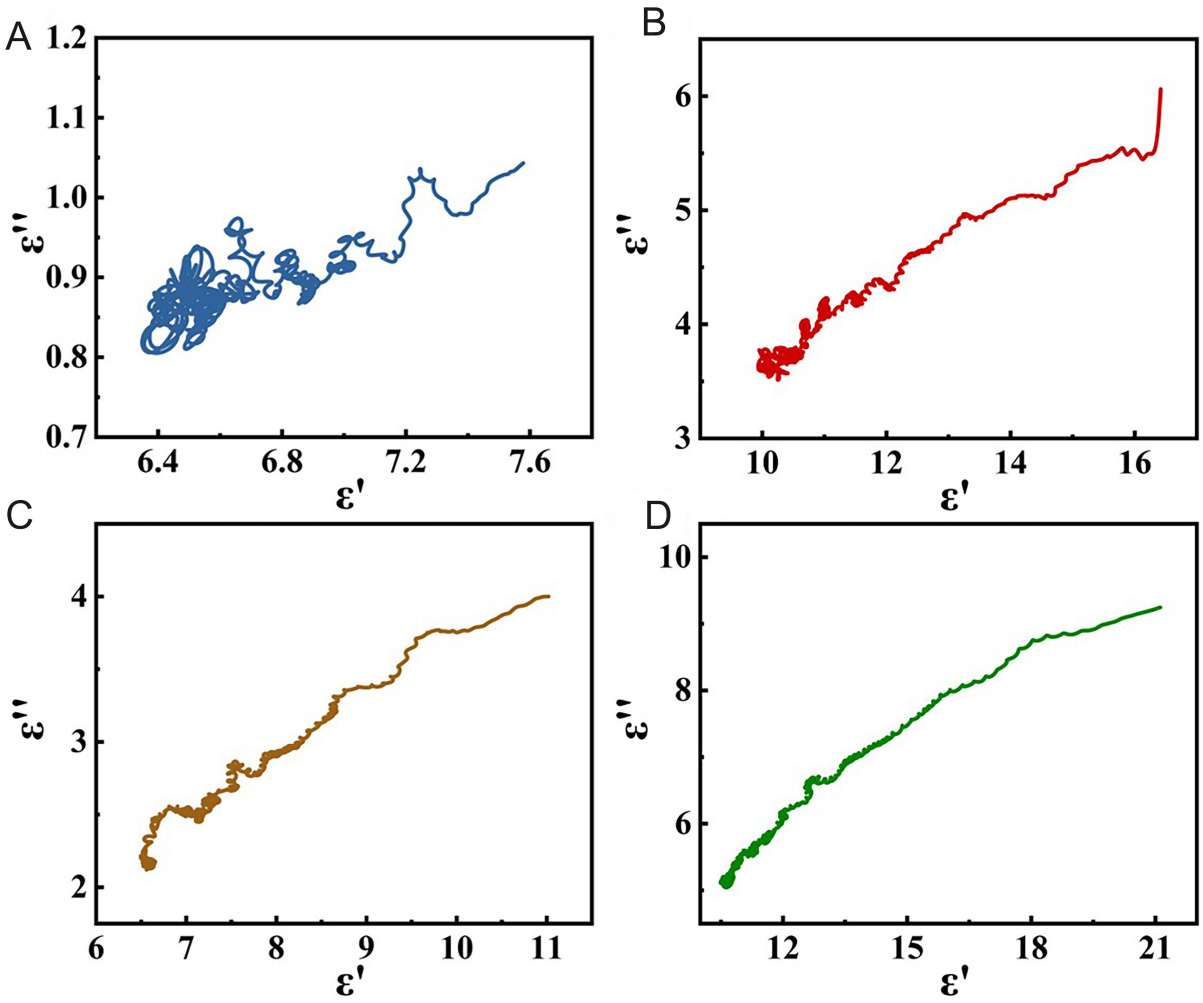

Figure 9. Cole-Cole semicircle curves of S1 (A), S2 (B), S3 (C), S4 (D).

supported by experimental and computational studies[48]. EMW radiation exposure of the composite surface induces the formation of interfacial space charge regions and local electric fields, thereby giving rise to free charge accumulation[24]. The free electron theory indicates that the emergence of relaxation peaks arises from the abnormal increase in local resistance. Furthermore, structural imperfections such as broken holes or cracks introduce edge effects, promoting the formation of additional dipoles[49]. Therefore, it can be inferred that conductive loss and interfacial polarization loss predominantly govern EMW dissipation in this case.

To further quantify the relative contributions of conduction loss and polarization loss, Debye relaxation fitting was performed on all samples. According to Debye theory, the total dielectric loss can be expressed as the sum of the conduction loss (ε''_c) and the polarization loss (ε''_p)[50]. Figure 10A and B display the frequency-dependent curves of ε''_c and ε''_p for the four samples over the 2-18 GHz range. The results indicate that both the conduction loss and polarization loss increase with rising annealing temperature. The enhancement in conduction loss is mainly attributed to the increase in metallic Ni content, which raises the electrical conductivity of the material. Additionally, as noted earlier, the carbon content of sample S3 is lower than that of S2, thus leading to a slight decrease in the conduction loss of S3. The growth in polarization loss primarily originates from the increased interfaces between metallic Ni and the ferrite, which strengthens the interfacial polarization effect.

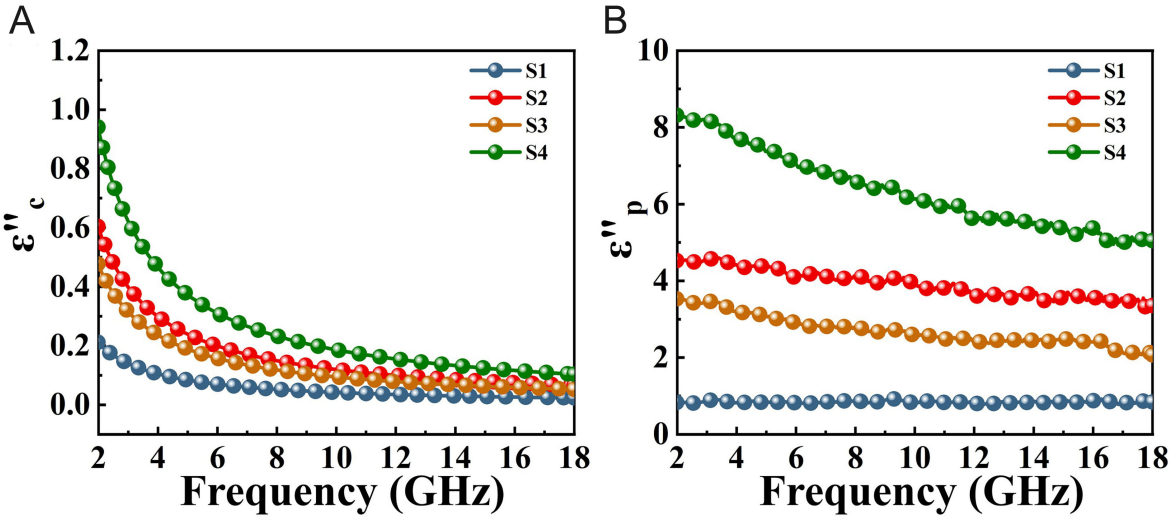

Figure 10. The separated ε''_c (A) and ε''_p (B) of S1, S2, S3, and S4 within the frequency range of 2-18 GHz.

Magnetic losses are mainly attributed to hysteresis and eddy current effects, along with the multiple resonance mechanisms (including exchange, domain wall, and natural resonance)[51]. Given their predominant occurrence at lower frequencies (MHz), domain wall resonance loss and hysteresis loss are negligible in this context. The eddy current loss is given by[52]:

$$C_0 = \mu'' (\mu')^{-2} f^{-1} = 2\pi\sigma d^2 \mu_0 \tag{3}$$

Here, σ and μ_0 are respectively the electrical conductivity and the vacuum permeability, while C_0 (ns) represents the eddy current coefficient. If the RL arises exclusively from eddy currents, then the C_0 values will exhibit no variation across the frequency spectrum. The C_0 values of all samples are presented in Figure 11A, the attenuation constant (α) is shown in Figure 11B, and the $|Z_{in}/Z_0|$ values are displayed individually in Figure 11C-F. Notably, the C_0 values of the S2, S3, and S4 show minimal variation across the 14-18 GHz frequencies, suggesting that eddy current losses dominate the magnetic loss within this spectrum. Meanwhile, across the 2-14 GHz range, magnetic loss is significantly reduced and is primarily characterized by exchange and natural resonance effects.

For the quantitative evaluation and comparison of absorber performance, the RL is calculated using transmission line theory, with the relevant equations given below[53]:

$$RL(dB) = 20log\left|(Z_{in} - Z_0)/(Z_{in} + Z_0)\right| \tag{4}$$

$$Z_{in} = Z_0\sqrt{\mu_r/\varepsilon_r}tan\ h\left[j(2\pi fd/c)\sqrt{\mu_r\varepsilon_r}\right] \tag{5}$$

Here, Z_{in} and Z_0 are the input impedance of the EMW absorbing materials and the impedance of free space, respectively; ε_r and μ_r represent the relative complex permittivity and permeability; c, f, and d correspond to the speed of light in the vacuum, the frequency of the EMW, and the absorber thickness.

In general, the RL value below -10 dB is defined as indicating effective EMW absorption, corresponding to an EMW absorption rate exceeding 90%. This is commonly used as the criterion for determining effective EMW absorption. Figure 12 depicts the RL curves for samples S1 through S4 across a thickness range of

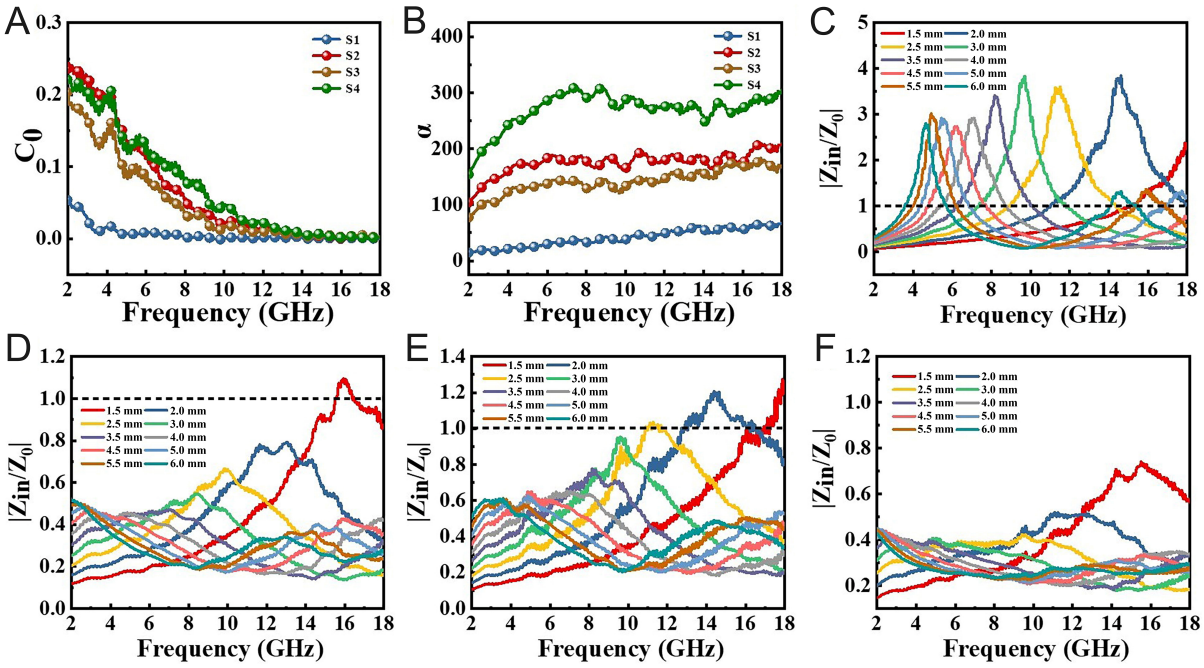

Figure 11. The values of C_0 (A) and attenuation constant α (B) of all samples, impedance matching conditions of S1 (C), S2 (D), S3 (E), S4 (F).

1.5 mm to 6.0 mm. Possessing an excellent RL and a broad EAB (RL ≤ -10 dB), sample S3 emerged as the best performer in EMW absorption among the four samples tested. Sample S3 delivers the strongest RL of -35.79 dB at 12.00 GHz with a 2.5 mm thickness (EAB: 4.12 GHz), and the widest EAB of 5.29 GHz at 2.0 mm, where the RL is -34.14 dB. For S2, the maximum RL is -32.30 dB (EAB: 3.09 GHz) at 1.5 mm, and -18.66 dB (EAB: 3.66 GHz) at 2.0 mm. S1 and S4 display weak performance, with peak RLs of only -21.44 dB at 6.0 mm (EAB: 1.84 GHz at 5.5 mm) and -15.86 dB at 1.5 mm (EAB: 3.84 GHz).

The RL peaks exhibited a consistent shift to lower frequencies with greater thickness. This trend is attributed to the quarter-wavelength model[54]:

$$t_m = \frac{n\lambda}{4} = nc/\left(4f_m\sqrt{|\mu_r||\varepsilon_r|}\right) \quad (n = 1, 3, 5\cdots) \tag{6}$$

Here, t_m, f_m, λ, and c represent the matching thickness, matching frequency, wavelength, and the speed of light in vacuum, respectively. Figure 12 plots the tm against the dm for samples S1-S4 at the $\lambda/4$ and $3\lambda/4$ wavelengths. The peak layer thickness for all samples matches well with the quarter wavelength, confirming that the quarter-wavelength cancellation model governs the microwave absorption mechanism.

The microwave absorption properties of materials are primarily determined by two key factors: impedance matching and electromagnetic attenuation. The impedance matching $|Z_{in}/Z_0|$, calculated using Equation (5) above, reflects the efficiency with which incident EMW enter the absorber and are subsequently converted into thermal energy[55]. The $|Z_{in}/Z_0|$ value close to 1 is a direct indicator of optimal impedance matching, thereby allowing a greater proportion of incident EMW to enter the material. In addition, good impedance matching enables the material to minimize the reflection of EMW at its surface. In Figure 11C-F, the $|Z_{in}/Z_0|$ curves for S2 and S3 approach 1, indicating well-matched impedance. However, since the $|Z_{in}/Z_0|$ values for S1 and S4 deviate from 1, the majority of the incident EMW undergoes reflection at the surface. Thus, S1 and S4 have poor absorption performance.

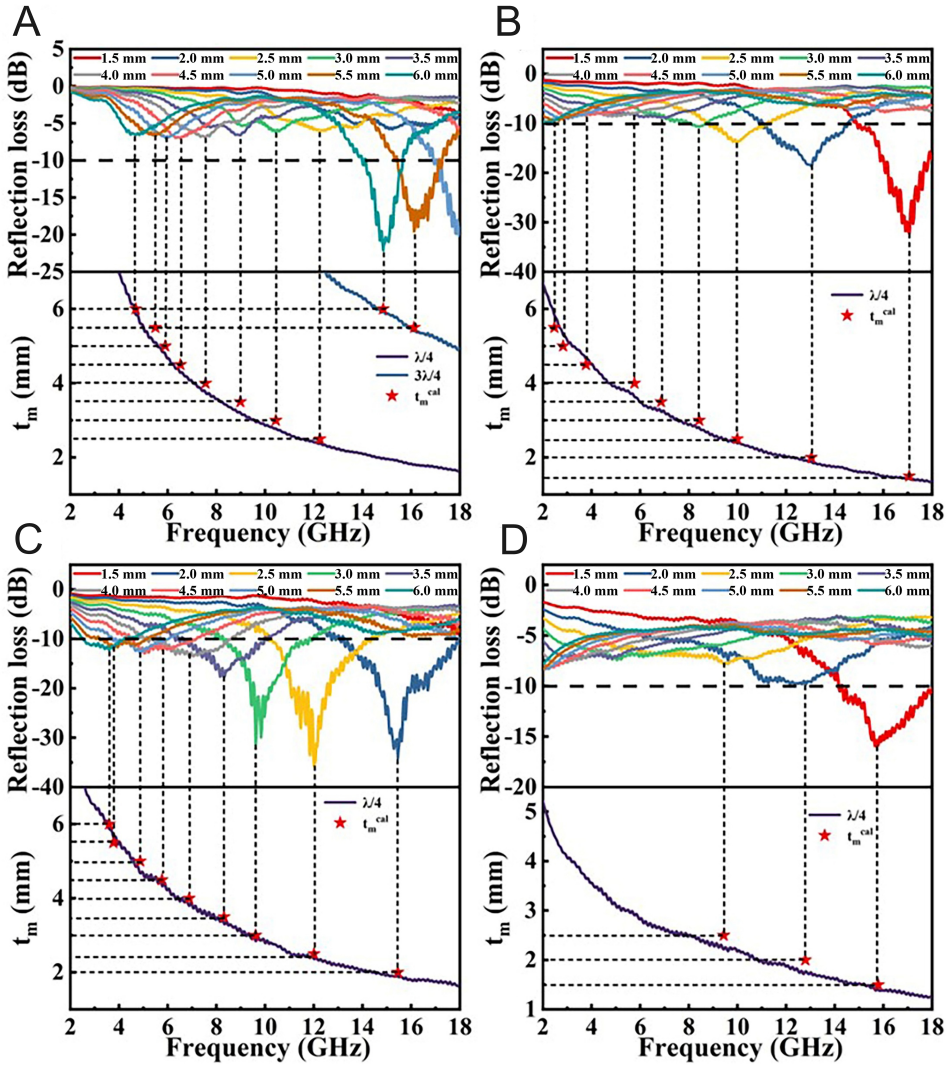

Figure 12. Frequency dependence of RL, matching thickness curves under $\lambda/4$ conditions of S1 (A), S2 (B), S3 (C), S4 (D). RL: Reflection loss.

The α can be estimated by the following formula[56]:

$$\alpha = \sqrt{2}\pi f/c \times \sqrt{(\mu''\varepsilon'' - \mu'\varepsilon') + \sqrt{(\mu''\varepsilon'' - \mu'\varepsilon')^2 + (\mu'\varepsilon'' + \mu''\varepsilon')^2}} \quad (7)$$

As shown in Figure 11B, α values of all samples show an increasing tendency as frequency varies. The α values follow the sequence S4 > S2 > S3 > S1. This order aligns with that of the tangent dielectric loss, underscoring the crucial role of dielectric loss[24]. The highest α value observed in S4 can be attributed to its higher ε'' and μ'' values. However, as the annealing temperature increases, the content of metallic Ni gradually increases, leading to an increase in material conductivity, enhanced surface reflection, and prevention of electromagnetic wave entry, resulting in deterioration of the impedance matching of S4. Therefore, based on the preceding impedance matching analysis, S3 is identified as the most promising absorbent candidate.

In addition, the $Ni_{0.5}Zn_{0.5}Fe_2O_4$/C/Ni microspheres, based on a hollow structure, can achieve excellent microwave absorption performance at low filling ratios, demonstrating the advantage of lightweight. Table 1 compares the filling ratios and microwave absorption performance of other ferrite-based materials.

Table 1. Microwave absorption properties and filling ratio of $Ni_{0.5}Zn_{0.5}Fe_2O_4$/C/Ni and other ferrite-based materials

Materials	RL_{min} (dB)	EAB (GHz)	Thickness (mm)	wt. (%)	Ref.
$Zn_{0.35}Ni_{0.65}Fe_2O_4$/Ni-Cu	-35	4.7	2	80	[57]
$NiFe_2O_4$/CF	-20.46	3.98	2.55	20	[58]
PNBC/$CoFe_2$/$CoFe_2O_4$	-52.21	4.32	1.44	30	[59]
$Mn_{0.8}Zn_{0.2}Fe_2O_4$/EMG4	-60 (1.77 mm)	4.56	1.47	70	[60]
Fe_3O_4@C	-53.7 (1.7 mm)	5.26	1.9	40	[61]
$Ni_{0.5}Zn_{0.5}Fe_2O_4$/C/Ni	-35.79 (2.5 mm)	5.29	2	20	This work

CF: Carbonized carbon; PNBC: pine needle biomass-derived carbon; EMG4: expanded microcrystalline graphite of 4%; EAB: effective absorption bandwidth.

The analysis shows that as the annealing temperature increases, the crystallinity of carbon in the samples is progressively enhanced, which in turn leads to improved electrical conductivity. Simultaneously, Ni elements progressively aggregate to form metallic particles. Consequently, when the annealing temperature reaches 800 °C, the content of metallic Ni reaches its peak, resulting in the highest dielectric loss for the S4 sample. However, this also compromises its impedance matching performance. In contrast, the S3 sample, benefiting from an optimal annealing temperature, achieves better control over carbonization degree and metallic Ni content. This results in a well-balanced dielectric loss capability and impedance matching performance, yielding a satisfactory attenuation constant. The mechanism of EMW loss in $Ni_{0.5}Zn_{0.5}Fe_2O_4$/C/Ni hollow microspheres primarily stems from the following factors. First, through the synergistic effect of controlling the metallic Ni content via annealing temperature and the hollow structure within the microspheres, $Ni_{0.5}Zn_{0.5}Fe_2O_4$/C/Ni hollow microspheres achieve excellent impedance matching. Second, the hollow architecture effectively reduces the sample weight, enabling the composite to achieve excellent microwave absorption at a low filling ratio, which is beneficial for lightweighting and broadens the application scope. Meanwhile, the hollow structure creates heterogeneous interfaces with air, thereby enhancing interfacial polarization. Structural defects such as fractured pores and cracks serve as additional dipole centers, giving rise to dipole polarization loss. Furthermore, conductive loss primarily attributed to carbon and natural resonance induced by the ferrite are also significant contributors. These characteristics collectively contribute to the realization of broadband absorption performance.

CONCLUSION

In summary, $Ni_{0.5}Zn_{0.5}Fe_2O_4$/C hollow microspheres were successfully fabricated through a simple two-stage method of hydrothermal and calcination. The study reveals that $Ni_{0.5}Zn_{0.5}Fe_2O_4$/C hollow microspheres annealed at 700 °C exhibit superior microwave absorption. The optimal performance includes an RL value of -35.79 dB at 2.5 mm, while with a thinner layer of 2.0 mm, it offers an EAB reaching 5.29 GHz. The excellent broadband absorption arises from the synergistic combination of interfacial polarization, dipole polarization, conduction loss, and natural resonance, facilitated by the hollow architecture, the graphitized carbon, and the formed metallic Ni. This research offers novel inspiration and perspectives for enhancing the performance of ferrite absorbers.

DECLARATIONS

Authors' contributions

Writing-original draft, writing-review & editing, conceptualization, data analysis: Zhou, D.; Wang, A.
Writing-review & editing, data analysis, funding acquisition: Gao, Y.
Data analysis & curation: Zhou, D.; Li, C.
Collecting literature, investigation, conceptualization: Shi, R.; Wu, Q.
Conceptualization, writing-review, funding acquisition: Man, Q.; Shen, B.

Availability of data and materials

The data presented in this study are available on request from the corresponding author due to privacy.

AI and AI-assisted tools statement

Not applicable.

Financial support and sponsorship

This work was supported by National Natural Science Foundation of China (Grant 62501580), Natural Science Foundation of Zhejiang Province (Grant LQN26F010009), and Natural Science Foundation of Ningbo [Grant 2024J430].

Conflicts of interest

Wu, Q. is affiliated with Ningbo Fengci Technology Co., Ltd., while the other authors have declared that they have no conflicts of interest.

Ethical approval and consent to participate

Not applicable.

Consent for publication

Not applicable.

REFERENCES

1. Derakhshani, M.; Taheri-Nassaj, E.; Jazirehpour, M.; Masoudpanah, S. M. Structural, magnetic, and gigahertz-range electromagnetic wave absorption properties of bulk Ni-Zn ferrite. *Sci. Rep.* **2021**, *11*, 9468. DOI PubMed PMC
2. Ding, D.; Wang, Y.; Li, X.; et al. Rational design of core-shell Co@C microspheres for high-performance microwave absorption. *Carbon* **2017**, *111*, 722-32. DOI
3. Zhao, D.; Lv, Q.; Shen, Z. Fabrication and microwave absorbing properties of Ni-Zn spinel ferrites. *J. Alloys. Compd.* **2009**, *480*, 634-8. DOI
4. Zhang, Y.; Gong, X.; Zeng, Y.; et al. An urchin-inspired broadband and ultralight microwave absorber. *Adv. Funct. Mater.* **2025**, *35*, 2419943. DOI
5. Xiang, L.; Qi, X.; Rao, Y.; et al. A simple strategy to develop heterostructured carbon paper/Co nanoparticles composites with lightweight, tunable and broadband microwave absorption. *Mater. Today. Phys.* **2023**, *34*, 101030. DOI
6. Xu, P.; He, H.; Qi, D.; Fu, L.; Yue, X.; Zhu, X. Egg white-derived carbon/magnetic nanoparticles/water-soluble graphene oxide composite with homogeneous structure as an excellent electromagnetic wave absorber. *J. Mater. Chem. C.* **2021**, *9*, 9292-301. DOI
7. Shao, C.; Liu, H.; Shi, Y.; Tian, N.; You, C.; Zhao, Z. Dielectric-magnetic synergy in ferrite/carbon composites for electromagnetic microwave absorption. *Nano. Res.* **2025**, *18*, 94907815. DOI
8. Guo, J.; Sun, Y.; Chen, Z.; et al. Electrostatic self-assembled ceramic magnetic $Ti_3C_2T_x$ nanocomposites reinforced with hollow Fe_3O_4 particles for strong and broadband absorption of electromagnetic waves. *Ceram. Int.* **2025**, *51*, 29283-91. DOI
9. Luo, N.; Ma, Y.; Ni, Z.; Chen, F.; Fu, Q. Preparation of reduced graphene oxide aerogel microspheres with excellent electromagnetic microwave absorption performance. *Carbon* **2025**, *243*, 120466. DOI
10. Wei, H.; Lei, T.; Li, W. Lightweight, flexible, heat resistant and thermal insulating aramid nanofiber/magnetic carbon nanotube interpenetrating network aerogel for microwave absorption in complex environments. *Carbon* **2024**, *225*, 119115. DOI
11. Zhu, S.; Huang, K.; Ni, J.; et al. Magnetic and microwave absorption properties of $Ni_{0.6}Zn_{0.4}Fe_2O_4/SrFe_{12}O_{19}$ composites. *Mater. Chem. Phys.* **2022**, *288*, 126398. DOI
12. Zhao, Q.; Liu, Y.; Rong, H.; et al. Ni-Zn 18H ferrite materials with abundant structural defects for waveband-tunable electromagnetic wave absorption. *Ceram. Int.* **2025**, *51*, 31917-25. DOI
13. Ibrahim, R. S.; Ahmad, M. M.; Azab, A. A. CuO/MFe_2O_4 (M = Co, Ni and Fe) ferrite nanocomposites: synthesis, characterization, optical and magnetic properties for diverse applications. *Appl. Phys. A.* **2025**, *131*, 9050. DOI
14. Wang, C.; Shen, Y.; Wang, X.; Zhang, H.; Xie, A. Synthesis of novel NiZn-ferrite/polyaniline nanocomposites and their microwave absorption properties. *Mater. Sci. Semicond. Process.* **2013**, *16*, 77-82. DOI

15. Wahaab, F. A.; Adebayo, L. L.; Rostami, A.; et al. Microwave absorption performance of $Ni_{0.5}Zn_{0.5}Fe_2O_4$ nanoclusters at 8.2-18 GHz frequency. *Indian. J. Phys.* **2022**, *96*, 723-33. DOI
16. Singh, S.; Chaudhary, P.; Srivastava, R.; Kant, Tripathi. R.; Kumar, R.; Yadav, B. Improved growth of nano tin ferrites with their decoration on carbon foam for wastewater treatment. *Environ. Nanotechnol. Monit. Manag.* **2021**, *16*, 100546. DOI
17. Bychanok, D.; Li, S.; Sanchez-sanchez, A.; et al. Hollow carbon spheres in microwaves: Bio inspired absorbing coating. *Appl. Phys. Lett.* **2016**, *108*, 013701. DOI
18. Tang, Y.; Yin, P.; Zhang, L.; et al. Novel carbon encapsulated zinc ferrite/MWCNTs composite: preparation and low-frequency microwave absorption investigation. *Ceram. Int.* **2020**, *46*, 28250-61. DOI
19. Zong, M.; Huang, Y.; Zhang, N. Reduced graphene oxide-$Ni_{0.5}Zn_{0.5}Fe_2O_4$ composite: synthesis and electromagnetic absorption properties. *Mater. Lett.* **2015**, *145*, 115-9. DOI
20. Zhou, X.; Shen, L.; Li, L.; et al. Preparation of nanocrystalline-coated carbon nanotube/$Ni_{0.5}Zn_{0.5}Fe_2O_4$ composite with excellent electromagnetic property as microwave absorber. *J. Phys. D. Appl. Phys.* **2013**, *46*, 145002. DOI
21. Li, Z.; Yang, Z. Microwave absorption properties and mechanism for hollow Fe_3O_4 nanosphere composites. *J. Magn. Magn. Mater.* **2015**, *387*, 131-8. DOI
22. Aslam, M. A.; Hu, K.; Ding, W.; et al. Dimensionality determined microwave absorption properties in ferrite/bio-carbon composites. *Ceram. Int.* **2021**, *47*, 27496-502. DOI
23. Bao, S.; Zhang, M.; Bu, X.; Zhang, W.; Jiang, Z.; Xie, Z. Combinatorial structural engineering of multichannel hierarchical hollow microspheres assembled from centripetal Fe/C nanosheets to achieve effective integration of sound absorption and microwave absorption. *ACS. Appl. Mater. Interfaces.* **2023**, *15*, 13565-75. DOI
24. Ge, J.; Liu, S.; Liu, L.; et al. Optimizing the electromagnetic wave absorption performance of designed hollow $CoFe_2O_4$/CoFe@C microspheres. *J. Mater. Sci. Technol.* **2021**, *81*, 190-202. DOI
25. Sui, M.; Sun, X.; Lou, H.; et al. Synthesis of hollow Fe_3O_4 particles via one-step solvothermal approach for microwave absorption materials: effect of reactant concentration, reaction temperature and reaction time. *J. Mater. Sci. Mater. Electron.* **2018**, *29*, 7539-50. DOI
26. Mandal, D.; Gorai, A.; Mandal, K. Electromagnetic wave trapping in $NiFe_2O_4$ nano-hollow spheres: an efficient microwave absorber. *J. Magn. Magn. Mater.* **2019**, *485*, 43-8. DOI
27. Zhu, X.; Dong, Y.; Pan, F.; et al. Covalent organic framework-derived hollow core-shell Fe/Fe_3O_4@porous carbon composites with corrosion resistance for lightweight and efficient microwave absorption. *Compos. Commun.* **2021**, *25*, 100731. DOI
28. Zhang, M.; Liu, Q.; Zi, Z.; et al. Magnetic and microwave absorption properties of $Ni_{1-x}Zn_xFe_2O_4$ nanocrystalline synthesized by sol-gel method. *Sci. China. Technol. Sci.* **2013**, *56*, 13-9. DOI
29. Xu, Y.; Xiong, S.; Weng, S.; et al. Rationally designed Ni_2P/Ni/C as a positive electrode for high-performance hybrid supercapacitors. *New. J. Chem.* **2020**, *44*, 6810-7. DOI
30. Okamura, M.; Takagaki, A.; Toda, M.; et al. Acid-catalyzed reactions on flexible polycyclic aromatic carbon in amorphous carbon. *Chem. Mater.* **2006**, *18*, 3039-45. DOI
31. Zhou, X.; Jia, Z.; Zhang, X.; et al. Controllable synthesis of Ni/NiO@porous carbon hybrid composites towards remarkable electromagnetic wave absorption and wide absorption bandwidth. *J. Mater. Sci. Technol.* **2021**, *87*, 120-32. DOI
32. Bhattacharjee, K.; Pati, S. P.; Das, G. C.; Das, D.; Chattopadhyay, K. K. Effect of particle size distribution on the structure, hyperfine, and magnetic properties of $Ni_{0.5}Zn_{0.5}Fe_2O_4$ nanopowders. *J. Appl. Phys.* **2014**, *116*, 233907. DOI
33. Anupama, M.; Rudraswamy, B.; Dhananjaya, N. Investigation on impedance response and dielectric relaxation of Ni-Zn ferrites prepared by self-combustion technique. *J. Alloys. Compd.* **2017**, *706*, 554-61. DOI
34. Gómez CA, Barrero Meneses CA, Jaén JA. Raman, infrared and Mössbauer spectroscopic studies of solid-state synthesized Ni-Zn ferrites. *J. Magn. Magn. Mater.* **2020**, *505*, 166710. DOI
35. Li, W.; Qi, H.; Niu, X.; et al. Fe-Fe_3C/C microspheres as a lightweight microwave absorbent. *RSC. Adv.* **2016**, *6*, 24820-6. DOI
36. Cheng, Y.; Zhao, H.; Yang, Z.; et al. An unusual route to grow carbon shell on Fe_3O_4 microspheres with enhanced microwave absorption. *J. Alloys. Compd.* **2018**, *762*, 463-72. DOI
37. Li, Z.; Lai, X.; Wang, H.; Mao, D.; Xing, C.; Wang, D. General synthesis of homogeneous hollow core-shell ferrite microspheres. *J. Phys. Chem. C.* **2009**, *113*, 2792-7. DOI
38. Hao, A.; Ismail, M.; He, S.; et al. Enhanced resistive switching and magnetic properties of Gd-doped $NiFe_2O_4$ thin films prepared by chemical solution deposition method. *Mater. Sci. Eng. B.* **2018**, *229*, 86-95. DOI
39. Zhai, Y.; Li, C.; Xu, G.; Ma, Y.; Liu, X.; Zhang, Y. Depolymerization of lignin via a non-precious Ni-Fe alloy catalyst supported on activated carbon. *Green. Chem.* **2017**, *19*, 1895-903. DOI

40. Yun, X.; Wu, Q.; Feng, L.; et al. Microwave absorption enhancement of e-Fe_3O_4@C microspheres by core surface modification. *J. Alloys. Compd.* **2020**, *835*, 155307. DOI
41. Liu, R.; Zhang, Y.; Duan, L.; Zhao, X. Effect of Fe^{2+}/Fe^{3+} ratio on photocatalytic activities of $Zn_{1-x}Fe_xO$ nanoparticles fabricated by the auto combustion method. *Ceram. Int.* **2020**, *46*, 1-7. DOI
42. Jia, Z.; Kong, M.; Yu, B.; Ma, Y.; Pan, J.; Wu, G. Tunable Co/ZnO/C@MWCNTs based on carbon nanotube-coated MOF with excellent microwave absorption properties. *J. Mater. Sci. Technol.* **2022**, *127*, 153-63. DOI
43. Liu, Y.; Li, Y.; Jiang, K.; Tong, G.; Lv, T.; Wu, W. Controllable synthesis of elliptical Fe_3O_4@C and Fe_3O_4/Fe@C nanorings for plasmon resonance-enhanced microwave absorption. *J. Mater. Chem. C.* **2016**, *4*, 7316-23. DOI
44. Wang, Y.; Xian, G.; Wu, C.; et al. Ultra-thin Ni@nitrogen-doped polyaniline-derived carbon composites with broadband electromagnetic wave absorption. *New. J. Chem.* **2023**, *47*, 17032-41. DOI
45. Zang, J.; Li, H.; Li, Z.; et al. Excellent microwave absorption of porous rod spinel by exceeding the Snoek limit *via* fibrosis and grain refinements. *J. Mater. Chem. C.* **2024**, *12*, 18458-71. DOI
46. Zhou, J.; Shu, X.; Wang, Y.; et al. Enhanced microwave absorption properties of (1-x)$CoFe_2O_4$/$_x$CoFe composites at multiple frequency bands. *J. Magn. Magn. Mater.* **2020**, *493*, 165699. DOI
47. Zhang, W.; Tan, G.; Hu, J.; Wang, Q.; Yan, W.; Man, Q. Enhancing electromagnetic wave absorption performance through co-regulation of microstructure and spatial orientation of RE-Ni MOF. *Chem. Eng. J.* **2023**, *478*, 147414. DOI
48. Luo, K.; Zhao, B.; Xu, C.; et al. Construction of one-dimensional hierarchical MoS_2/Ni_3S_2 composites with enhanced interfacial polarization and improved wideband microwave absorption. *J. Mater. Sci. Technol.* **2024**, *178*, 22-8. DOI
49. Yang, P.; Deng, W.; Ruan, H.; et al. Amorphous/Graphitic carbon phase engineering of corrosion-resistant Fe@C Core-Shell nanowires for optimized dipole polarization and enhanced microwave absorption. *Chem. Eng. J.* **2024**, *492*, 152253. DOI
50. Gao, Y.; Wu, Q.; Jia, X.; et al. Orientation architecture engineering for enhanced electromagnetic wave absorption and active-passive infrared camouflage performances. *Adv. Funct. Mater.* **2025**, *35*, 2508442. DOI
51. Pan, J.; Guo, H.; Wang, M.; et al. Shape anisotropic Fe_3O_4 nanotubes for efficient microwave absorption. *Nano. Res.* **2020**, *13*, 621-9. DOI
52. Zhang, N.; Huang, Y.; Wang, M. 3D ferromagnetic graphene nanocomposites with ZnO nanorods and Fe_3O_4 nanoparticles co-decorated for efficient electromagnetic wave absorption. *Compos. Part. B. Eng.* **2018**, *136*, 135-42. DOI
53. Zhang, M.; Qiu, J.; Xin, Z.; Sun, X. In situ reduced multi-core yolk-shell Co@C nanospheres for broadband microwave absorption. *Materials* **2021**, *14*, 4610. DOI
54. Wang, T.; Chen, G.; Zhu, J.; Gong, H.; Zhang, L.; Wu, H. Deep understanding of impedance matching and quarter wavelength theory in electromagnetic wave absorption. *J. Colloid. Interface. Sci.* **2021**, *595*, 1-5. DOI
55. Gai, L.; Zhao, Y.; Song, G.; et al. Construction of core-shell PPy@MoS_2 with nanotube-like heterostructures for electromagnetic wave absorption: Assembly and enhanced mechanism. *Compos. Part. A. Appl. Sci. Manuf.* **2020**, *136*, 105965. DOI
56. Huang, X.; Zhang, J.; Rao, W.; Sang, T.; Song, B.; Wong, C. Tunable electromagnetic properties and enhanced microwave absorption ability of flaky graphite/cobalt zinc ferrite composites. *J. Alloys. Compd.* **2016**, *662*, 409-14. DOI
57. Yan, L.; Men, W.; Zhang, Y.; et al. Frequency-tunable microwave absorption via balanced impedance matching in $Zn_{0.35}Ni_{0.65}Fe_2O_4$/Ni-Cu multiphase ferrite composites. *J. Alloys. Compd.* **2025**, *1035*, 181614. DOI
58. Bala, M.; Shivling, V.; Tyagi, S. Enhancing X-band microwave absorption properties with nickel ferrite and carbon-based composites. *Ceram. Int.* **2024**, *50*, 34123-32. DOI
59. Ji, X.; Deng, Y.; Xu, Z.; Chen, F. Facile synthesis of pine needle-derived carbon/$CoFe_2$/$CoFe_2O_4$ composites with precisely tunable microwave attenuation efficiency. *Mater. Today. Nano.* **2025**, *32*, 100707. DOI
60. Zhang, Y.; Wei, S.; Wang, B.; Liu, M.; Wang, Y.; Guo, L. Scalable mechanochemical synthesis of bifunctional MnZn ferrite/expanded graphite composites for efficient microwave absorption and corrosion resistance. *J. Mater. Chem. C.* **2026**, *14*, 743-53. DOI
61. Xu, J.; Liu, Z.; Li, Q.; et al. Wrinkled Fe_3O_4@C magnetic composite microspheres: regulation of magnetic content and their microwave absorbing performance. *J. Colloid. Interface. Sci.* **2021**, *601*, 397-410. DOI